Bio-Design and Manufacturing (2020) 3:189–202
https://doi.org/10.1007/s42242-020-00074-8

RESEARCH ARTICLE

A hepatocellular carcinoma–bone metastasis-on-a-chip model for studying thymoquinone-loaded anticancer nanoparticles

Fatemeh Sharifi[1,2] · Ozlem Yesil-Celiktas[1,3] · Aslihan Kazan[3] · Sushila Maharjan[1] · Saghi Saghazadeh[1] · Keikhosrow Firoozbakhsh[2] · Bahar Firoozabadi[2] · Yu Shrike Zhang[1]

Received: 26 February 2020 / Accepted: 16 April 2020 / Published online: 13 May 2020

Abstract

We report the development of a metastasis-on-a-chip platform to model and track hepatocellular carcinoma (HCC)–bone metastasis and to analyze the inhibitory effect of an herb-based compound, thymoquinone (TQ), in hindering the migration of liver cancer cells into the bone compartment. The bioreactor consisted of two chambers, one accommodating encapsulated HepG2 cells and one bone-mimetic niche containing hydroxyapatite (HAp). Above these chambers, a microporous membrane was placed to resemble the vascular barrier, where medium was circulated over the membrane. It was observed that the liver cancer cells proliferated inside the tumor microtissue and disseminated from the HCC chamber to the circulatory flow and eventually entered the bone chamber. The number of metastatic HepG2 cells to the bone compartment was remarkably higher in the presence of HAp in the hydrogel. TQ was then used as a metastasis-controlling agent in both free form and encapsulated nanoparticles, to analyze its suppressing effect on HCC metastasis. Results indicated that the nanoparticle-encapsulated TQ provided a longer period of inhibitory effect. In summary, HCC–bone metastasis-on-a-chip platform was demonstrated to model certain key aspects of the cancer metastasis process, hence corroborating the potential of enabling investigations on metastasis-associated biology as well as improved anti-metastatic drug screening.

Keywords Tumor-on-a-chip · Organ-on-a-chip · Hydroxyapatite · Hepatocellular carcinoma · Thymoquinone

Introduction

Cancer is one of the leading causes of death worldwide [1, 2]. It is anticipated that by 2030, approximately 22 million new patients will suffer from cancer and mortality will rise up to 13 million deaths annually [1]. Although enormous achievements in better understanding of the different mechanisms to diagnose and treat primary tumors, metastases are still the main reason of high mortality in cancer [2]. In metastasis, a cancer cell enters through endothelial barrier the surrounding blood stream or lymph node from its primary site, translocates to other parts of the body, extravasates from the microvasculature to the new site, and finally proliferates again to create new colonies [2]. Control and inhibition of cancer progression are therefore critical procedures in treating cancer.

Cellular composition, extracellular matrix (ECM), and blood circulation have prominent roles in affecting the metastasis of cancerous cells [2]. Due to the significant role of metastasis in the process of the cancer development and the lack of knowledge relating to its mechanism, various experimental models have been designed to better understand the specific roles of these parameters and reproduce and find treatments for the complicated metastasis cascade [2]. Among these different models, conventional in vitro static cell cultures usually fail to replicate the cellular behaviors in their native three-dimensional (3D) microenvironments [2].

Electronic supplementary material The online version of this article (https://doi.org/10.1007/s42242-020-00074-8) contains supplementary material, which is available to authorized users.

✉ Bahar Firoozabadi
Firoozabadi@sharif.edu

✉ Yu Shrike Zhang
yszhang@research.bwh.harvard.edu

1 Division of Engineering in Medicine, Department of Medicine, Brigham and Women's Hospital, Harvard Medical School, Cambridge, MA, USA

2 School of Mechanical Engineering, Sharif University of Technology, Tehran, Iran

3 Department of Bioengineering, Faculty of Engineering, Ege University, Bernova, Izmir, Turkey

Results obtained from animal models, on the other hand, may not be necessarily generalized to human pathophysiology because of the intrinsic interspecies differences [2–4]. To this end, microfabrication technologies have enabled the creation of biomimetic tissue and cancer models to bridge the gap of the conventional cell cultures and the human system by providing means to incorporate 3D niches with substantial cell–cell interactions and spatiotemporal gradients [2]. These on-chip 3D and dynamic models can be meticulously tuned and tightly controlled for their configurations to scrutinize various parameters in modeling cancer metastasis in vitro [2, 5].

Liver cancer can be classified into two main categories, i.e., primary and secondary. In the first category, liver cells become cancerous due to reasons such as hepatitis B or C virus infection or alcohol abuse [6]. Contrarily, in secondary liver cancer, cancerous cells are disseminated from another organ (primary site) to the liver [6]. In particular, hepatocellular carcinoma (HCC) is a common type of primary liver cancer considered as one of the most progressive cancers with a high mortality rate [7]. HCC has a strong metastatic potential, where the lung, lymph nodes, bone, and other intra-abdominal organs are key locations at risk of its metastasis [7]. Bone is a common metastasis site during HCC progression [7], and understanding its cause and screening treatment strategies would be strongly desired through generation of improved in vitro HCC–bone metastatic models.

Despite growing research in the development of cancer-on-a-chip models, recapitulating metastasis on these microfluidic devices is still in the infancy [5, 8]. Recently, in vitro systems have been used in modeling the metastasis cascade [9]. Since myriad parameters are involved in cancer metastasis, providing an in vitro model representing the metastasis process, even in its reduction form, can bring new insights to understand, predict, and control this cancer progression mechanism. Reported metastasis-on-a-chip models include separate compartments for primary and secondary tumor sites enabling control over parameters affecting tumor cell migration and real-time monitoring of the cancer invasion process. For example, cancer cell migration from colon cancer organoids to liver organoids was investigated under constant perfusion and results were compared to non-metastatic colon cancer [9]. Metastatic colon cancer cells were observed in the liver organoids, while non-metastasis colon cancer cells proliferated in their native site and did not translocate to the liver organoids. Breast cancer-to-bone metastasis-on-a-chip was developed, and it was shown that host chemokines had a great impact on attracting tumor cells toward the bone microtissue [10]. Microfluidics-based analysis of the effects of the bone microenvironment on prostate cancer cells was studied relating to signaling mechanisms, where modulated prostate cancer progression was observed by adding a bone-related protein osteopontin to the hydrogel [11]. Additional research further focused on investigating circulating tumor cells on interconnected multi-organ systems to mimic organ-specific cancer progression [5].

Moreover, microfluidic devices have been widely used as a tool for preclinical drug screening [2, 9]. Various organ-on-a-chip platforms have served to scrutinize the pharmaceutical effects of anticancer drugs [2, 12]. Due to the important role of the liver in drug metabolism pathways inside the body, liver-on-a-chip models are often linked to other organ models in drug studies [12]. Nevertheless, utilization of liver-on-a-chip systems has been mainly focused on drug screening or investigation of liver as a secondary host for other tumor cells. Studies on liver cancer, including HCC, on the chips albeit their importance and prevalence, have been rare. Also, despite these recent efforts in modeling cancer metastasis-on-a-chip, few of the previously reported studies investigated the effect of anti-metastatic treatments on hepatic cancer progression.

Here, we report the design of an on-chip model of primary HCC–bone metastasis. HepG2 cells were cultured in a biomimetic 3D hydrogel microenvironment to emulate the hepatic cancerous tissue, in one compartment of the dual-chamber microfluidic chip. In the other compartment of the chip parallel to the HCC tissue, a bone-mimetic niche, consisting of a 3D hydrogel matrix containing the bone mineral hydroxyapatite (HAp), was created. Above the two chambers, a microporous polymer membrane functioning as the physical vascular barrier was sandwiched in between the two bottom compartments and a common vascular chamber on top, with medium circulating during the culture period. Cancerous cells may recognize calcium ions released from the bone ECM via their calcium-sensing receptors and/or calcium-binding proteins [13]. Such signaling activates several pathways and attracts metastatic cancer cells toward the bone as they travel through the blood stream [7, 14]. We therefore hypothesized that the HCC cells in their primary chamber would sense the calcium ions released from the other chamber containing HAp and start to transmigrate across the vascular barrier to settle in the secondary bone-mimetic site, modeling the metastasis process in the human body, in a mineral-dependent manner.

Upon generation of the HCC–bone metastasis model, we subsequently explored the effect of pharmaceutical compounds in suppressing such metastasis. Specifically, an herb-derived compound thymoquinone (TQ) was used as a metastasis-controlling agent as TQ has been reported to prohibit cancerous cell invasion and metastasis [15] and reduce proliferation of a variety of cancer cell lines such as colon, liver, ovarian, and lung [15]. Since TQ is extracted from the herb *Nigella sativa*, it potentially has less side effects in comparison with other synthetic compounds used in chemotherapy and metastasis inhibition while increasing liver functionality [15]. Specifically, TQ was delivered

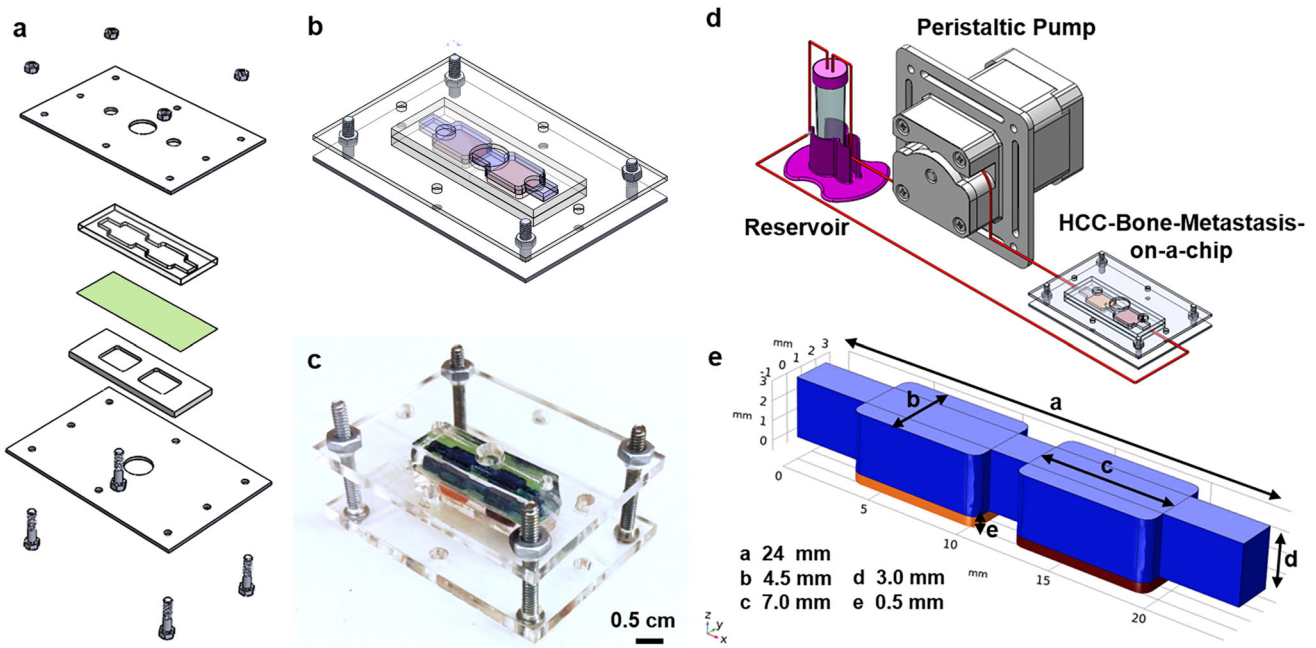

Fig. 1 HCC–bone metastasis model. **a** Schematic showing different components of the bioreactor. The blue parts are made of PDMS. The brown layer shows the transmembrane with a pore size of 3 μm. All parts are clamped with two PMMA holders and tightened with bolts and screws. **b** Schematic showing the assembled bioreactor. **c** Photograph showing the assembled bioreactor. The two bottom chambers are filled with orange and brown dyes. The green layer resembles the membrane, and the top fluidic chamber is filled with a blue dye. **d** Schematic showing the operation of the whole system where the assembled bioreactor is connected to the reservoir and peristaltic pump. **e** Schematic of the microfluidic chamber with sizes of all parts used in numerical simulations noted

to the HCC–bone metastasis microfluidic platform through medium perfusion in the vascular chamber, both in free form and encapsulated in nanoparticles. The effect of each configuration on HCC metastasis was analyzed.

Materials and methods

Bioreactor design and fabrication

The bioreactor (Fig. 1a, b) was made of two polydimethylsiloxane (PDMS, Sylgard 184 Elastomer Kit, Dow Corning, USA; weight ratio of monomer/crosslinker = 10:1) layers, sandwiching a 3-μm polyethylene terephthalate membrane (PET, Thermo Fisher, USA) in the middle mimicking the vascular barrier. The bioreactor was clamped by a pair of poly(methyl methacrylate) (PMMA) holders to ensure hydraulic tightness. A photograph of the actual bioreactor is shown in Fig. 1c, where orange indicates the HCC chamber, brown indicates the HAp compartment, blue represents the top vascular chamber, and green is the membrane (vascular barrier). The bioreactor was connected to a 5-mL reservoir, and a peristaltic pump (MP^2) was used to circulate the medium (Fig. 1d). The reservoir was placed before the bioreactor so that it could also serve as the bubble trap preventing the bubbles from entering the circulatory system [3]. The entire system was placed inside an incubator at 37 °C and 5% CO_2 for up to 21 days and examined regularly under a fluorescence microscope (Axio Observer D1, Carl Zeiss, Germany).

Hydrogel synthesis

Gelatin methacryloyl (GelMA) was used as the ECM–mimicking matrix for constructing HCC and bone-like tissues. GelMA has been widely used in tissue engineering and modeling including cancer cell cultures and bone tissue formation [16, 17]. GelMA was synthesized according to established protocol [16].

Hydrogel preparation

Hydrogel pre-polymer solution used in this experiment contained 5 wt% GelMA and 0.5 wt% photoinitiator (hydroxy-1-(4-(hydroxyethoxy)phenyl)-2-methyl-1-propanone (Sigma-Aldrich). Crosslinking was achieved at 8-cm distance from a UV light (Omnicure, Canada) with a power density of 45 mW cm^{-2} for 40 s to form GelMA hydrogels.

Cell culture and encapsulation

Human HepG2 HCC cells (ATCC, USA) were cultured in Dulbecco's modified Eagle's medium (DMEM, Thermo Fisher) supplemented with 10 vol% fetal bovine serum (FBS, Thermo Fisher) and 1 vol% penicillin–streptomycin (Thermo Fisher). Cultured cells were maintained in a standard condition at 37 °C and 5% CO_2. The cells were detached from the surface of the culture flasks using 1 vol% trypsin–EDTA treatment (Thermo Fisher) for approximately 5 min at 37 °C. The cells were re-suspended in the GelMA hydrogel pre-polymer solution, filled into the chamber, and photocrosslinked. To follow cell migration under fluorescence microscope when necessary, HepG2 cells were pre-labeled via cell tracker (CM Dil Dye, Thermo Fisher) according to manufacturer's instructions.

Cell metabolic activity and viability analyses

To analyze cell metabolic activity and viability, Presto Blue and Live/Dead assays were used. Medium was aspirated, and a solution containing the Presto Blue reagent (Thermo Fisher) and culture medium at a ratio of 1:10 was added to the cells in each well and kept for 30 min at 37 °C. Then, the medium over the cells was collected and measured by a plate reader (BioTeK, USA) at 569-nm excitation and 589-nm emission wavelengths. For qualitative analysis of cell viability, encapsulated cells were treated with a Live/Dead kit (Thermo Fisher) for 15 min at 37 °C. Under fluorescence microscope, live and dead cells were shown in green and red, respectively.

Numerical simulation

A 3D model of flow and oxygenation was set up using finite element analysis by Comsol Multiphysics 3.5a (COMSOL Inc., USA), in which mass, momentum of fluid flow, and oxygen transfer in the bioreactor were obtained to calculate shear stress and oxygen concentration inside the bioreactor. The dimensions of the bioreactor chamber are given in Fig. 1e. Medium inside the bioreactor was modeled as steady, incompressible, isothermal, Newtonian fluid. Fluid flow entered the microchannel through the inlet connection and was transferred via constant perfusion through the entire chamber. Continuity, Navier–Stokes, and Brinkman equations were solved to acquire velocity distribution inside the microfluidic chamber and the porous medium (i.e., the hydrogel matrix), respectively. Reynolds number (Re) for this model was $\mathrm{Re} \ll 1$, and therefore, the flow regime was considered laminar and the inertial terms of stated equations could be neglected. The equations related to this part are given in supplementary material.

Results

Hydrodynamics and oxygenation

HCC cells were encapsulated inside the GelMA hydrogel, providing a favorable 3D microenvironment for the encapsulated cells to survive, proliferate, and differentiate. In particular, GelMA with medium degree of methacryloyl substitution at a 5 wt% concentration was chosen for our HCC model construction since the stiffness of its UV-crosslinked hydrogel would be matching that of human liver cancer tissue [18], potentially providing the HepG2 cells with a biomimetic 3D niche. Cells at the concentration of 1×10^6 mL^{-1} were encapsulated to investigate HCC cell behaviors in the GelMA matrix and observe the effect of UV exposure on cells (Fig. S1a). Cell distribution was almost homogenous and the GelMA hydrogel maintained its integrity after 7 days of culture. Viability of the cells inside GelMA along the culture was analyzed with Live/Dead assay, which indicated high viability of the HCC cells inside the GelMA hydrogel throughout the 7-day culture period (Fig. S1b–d).

Fluid flow simulation inside the bioreactor was further conducted, where a parabolic velocity profile was clearly observed (Fig. S1e). Since inlet fluid flow was low and dimensions of the fluidic channel were small, Re for this flow was approximately 7×10^{-2}. Therefore, fluid flow regime was laminar and streamlines were obtained as shown in Fig. S1f. The velocity was chosen based on the flow pattern and sufficient oxygen delivery to the cells. In case of low velocity, hepatocytes could not receive adequate oxygen. Distribution of oxygen concentration inside the bioreactor was also simulated. The left bottom chamber contained HCC cells, which would consume oxygen. Hypoxia is anticipated to occur when available oxygen concentration of the cells falls below 1.0×10^{-4} mol m^{-3} [19]. However, as HCC is usually highly vascularized, we decided to model it on our chip under the normoxic condition. Perfusion velocity of 5 μL min^{-1} was thus chosen to supply the HCC cells with sufficient oxygen (Fig. S1g).

Optimization of HepG2 cell culture in GelMA

The effect of concentration of HepG2 cells inside the GelMA matrix was first examined under static culture in the bioreactor (Fig. 2). Cell viability on days 1, 3, and 7 with cell densities of 2×10^6, 3×10^6, and 5×10^6 cells mL^{-1} was measured using live/dead staining showing eminent ratios of live cells (green) with respect to dead cells (red) during the entire culture period under all conditions. HepG2 cell distribution on day 1 was almost homogenous for all cell densities. The cells started to proliferate and aggregate by producing spheroids of varying sizes in the GelMA matrix as clearly seen on day 7 (Fig. 2c, g, k). Cell metabolic activities were

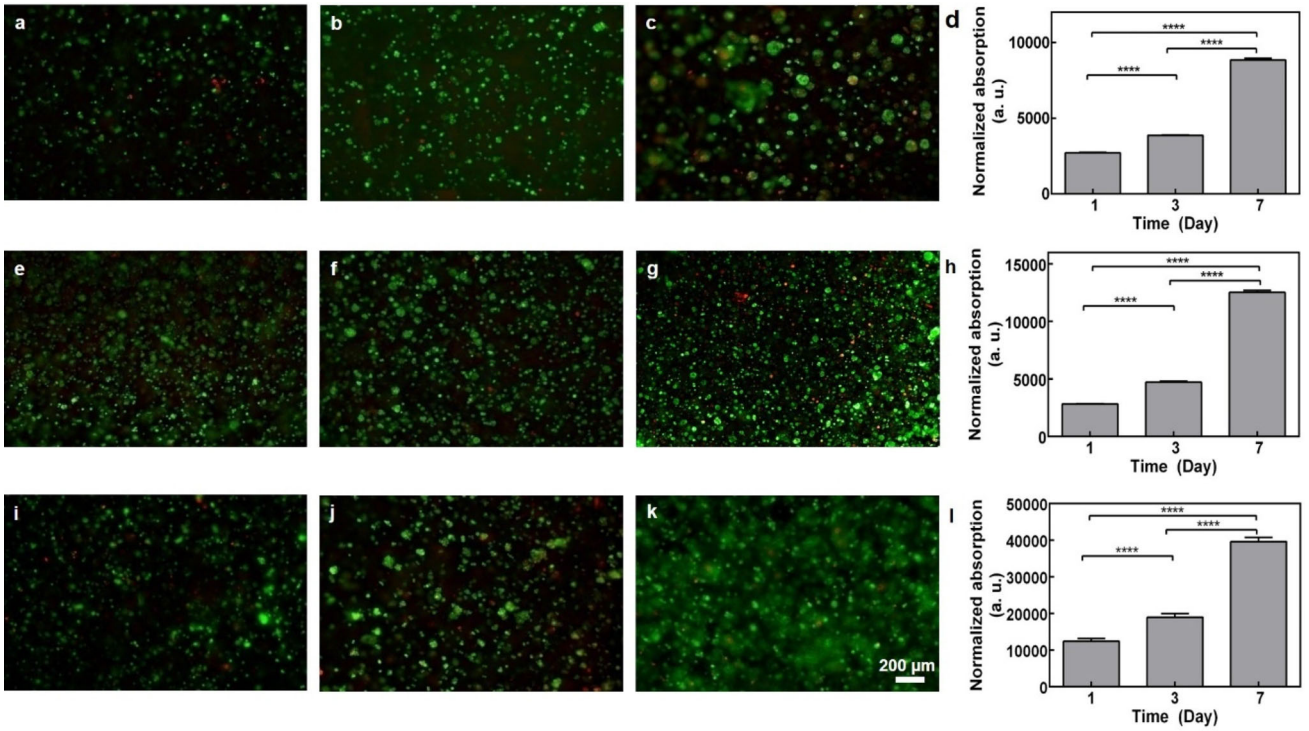

Fig. 2 HCC cell growth inside the chamber over time. **a–c** Live/dead staining for cell density at 2×10^6 after **a** day 1, **b** day 3, and **c** day 7. **d** Quantification of cell proliferation. **e–g** Live/dead staining for cell density at 3×10^6 after **e** day 1, **f** day 3, and **g** day 7. **h** Quantification of cell proliferation. **i–k** Live/dead staining for cell density at 5×10^6 after **i** day 1, **j** day 3, and **k** day 7. **l** Quantification of cell metabolic activities (***$P < 0.0001$)

also quantified using the Presto Blue assay (Fig. 2d, h, l), indicating the growth of the HepG2 cells during the 7-day culture period. Chemoattractant signaling has been shown as an important factor in promoting HCC cell motility and metastasis [7, 14]. To provide a similar microenvironment with the HCC native niche, a highly concentrated cellular environment might be needed to facilitate the generation of the HCC metastasis model. However, further increasing the cell density would result in too many cells during the culture period interfering with microscopic observation. Thereupon, 5×10^6 cells mL^{-1} was chosen since this high concentration seemed to also exhibit good cell viability and proliferation in our setup.

HCC metastasis-on-a-chip under flow and microenvironmental stimuli

Primary liver cancer, similar to the other cancer types, is under the influence of their surrounding microenvironmental stimuli by which it is induced to migrate to the secondary sites [7, 14]. It has been recognized that one of the frequent extrahepatic metastasis sites is the bone [7]. Bone provides an active microenvironment in conjunction with cellular interactions between the host bone and the hepatic cancerous cells [20]. Hence, the chemical signaling between the host tissue and the liver cancer cells, including the HepG2 cells used in our model, can be a dominant factor in attracting HCC–bone metastasis. Specifically, HAp is a natural biomineral occupying the majority of the normal bone ECM [20], which contains a high level of calcium ions. To this end, it is rationally assumed that HAp might be an effective component existing in the bone significantly contributing to bone metastasis of HCC.

To mimic the bone niche inside our model, HAp was encapsulated within the GelMA matrix in the second compartment at the bottom of the bioreactor. The effect of HAp concentration on cell viability was first examined under the static condition for up to 7 days (Fig. S2a). It could be observed that in all cases, in the presence of HAp inside the second chamber, the viability of the HepG2 cells also increased over time, indicating that HAp did not exert noticeable toxicity on these cells. As the natural bone ECM has much more mineral than our highest HAp concentration tested, it would be intuitive that the higher HAp embedded in the bone-like niche the better. However, in cases where HAp at even higher concentrations (>0.1 wt%) were used, the entire chamber became opaque leading to inability of observation under the microscope. The overly high concen-

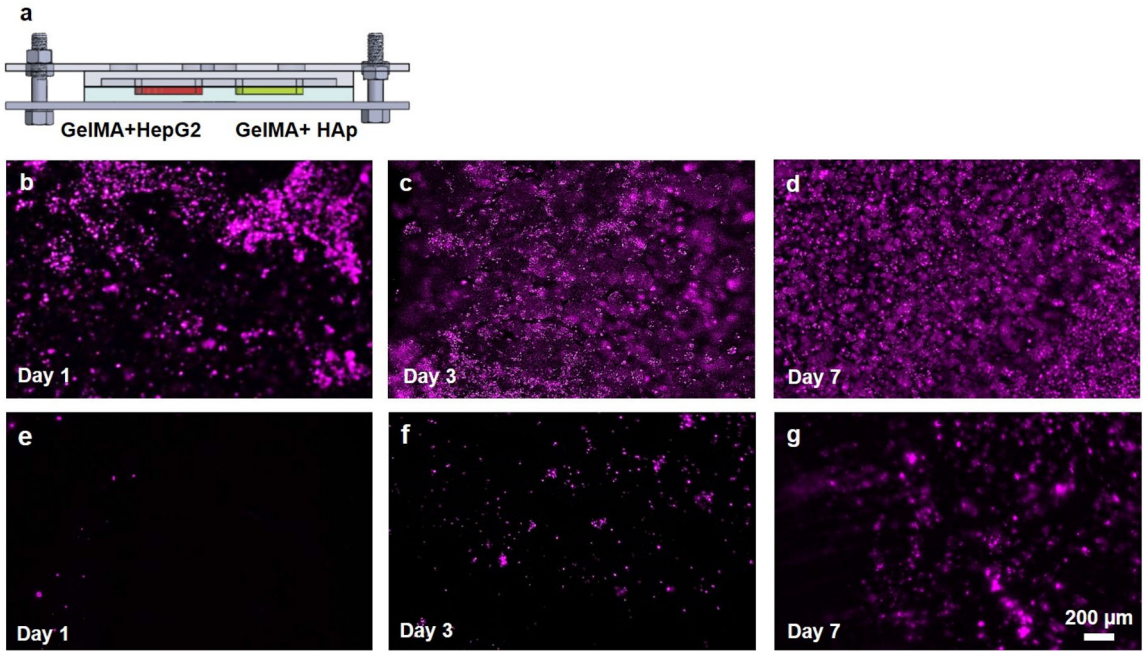

Fig. 3 HepG2 cell proliferation and metastasis to the HAp chamber under dynamic condition. **a** Schematic representation of the bioreactor configuration. **b–d** HepG2 cells encapsulated in GelMA inside left chamber on **b** day 1, **c** day 3, and **d** day 7. **e–g** cells migrated to/proliferated in the right chamber containing GelMA and 0.1 wt% HAp on **f** day 1, **g** day 3, and **h** day 7

tration of HAp also impaired the GelMA hydrogel formation. Consequently, GelMA containing HAp at a concentration of 0.1 wt% was adopted as the optimum formulation for further experiments.

In the first set of experiments, HCC metastasis under the effect of HAp was investigated under the dynamic condition. To mimic the HCC-to-bone metastasis inside the body, HepG2 cells tagged with cell tracker were encapsulated in GelMA in the left chamber and in the right chamber GelMA laden with HAp was placed, on top of which a PET membrane was sandwiched between the two PDMS layers (Fig. 3a). This porous membrane could effectively function as the vascular barrier [3] to mimic the HCC metastasis process in the human body. It was anticipated that the concentration of HepG2 cells inside the GelMA in the HCC chamber was sufficiently high so that the cells tended to leave this primary site to cross the vascular barrier as they proliferated. Additionally, the circulating HepG2 cells would sense the chemical stimuli, i.e., the locally concentrated calcium ions released from the bone niche received in the vascular chamber, and subsequently migrate across the porous membrane again to settle at the metastatic bone site, emulating the scenario how HCC (or many other cancer) metastasis occurs in the native situation. The bioreactor was run for up to 7 days and cell migration was examined microscopically (Fig. 3b–g) and quantified (Fig. 5c, e). Indeed, it was clear that metastasis of the HepG2 cells increased with respect to time. The results indicated a considerable cell migration into the HAp chamber demonstrating a metastasis-favorable environment for the circulating HCC cells to settle.

In parallel to the abovementioned setup, the bioreactors were also run with pure GelMA (no HAp) in the second chamber as the control (Figs. 4, 5d, f). From Fig. 4b–d, proper growth and viability of HCC cells could be observed suggesting the expedient environment for cell proliferation. By comparing these two sets of observations (Figs. 3, 4, 5), it could be inferred that including HAp in the second chamber, cell metastasis would be promoted and cell migration enhancement was more prominent after the third day possibly due to the locally released Ca^{2+} ions as the attractant. For example, the count of migrated cell was almost threefold more in the bioreactors with HAp in comparison with its counterpart, i.e., those without HAp, on day 3.

TQ toxicity on HCC cells

TQ is a natural anticancer and metastasis-prohibitive substance directly extracted from an herb *Nigella sativa* [15]. It was shown that the growth-inhibitory effect of TQ would specifically prevent cancer cell proliferation while not affecting other healthy cells [15]. Effect of TQ on hepatocarcinogenesis was also studied, and it was demonstrated that growth and viability of hepatic cancerous cells were considerably decreased [15]. As a start, TQ at an initial concentration

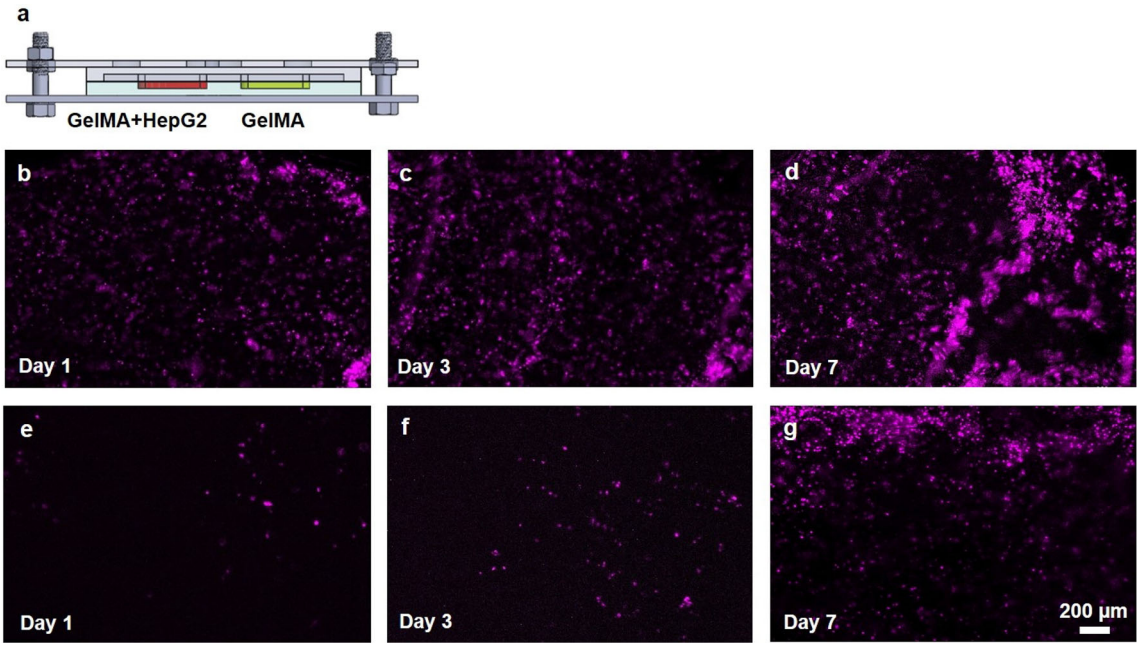

Fig. 4 HCC cell distribution and metastasis-on-chip in dynamic environment without HAp. **a** Schematic representation of the bioreactor. **b**–**d** HepG2 cells encapsulated in GelMA inside left chamber on **b** day 1, **c** day 3, **d** day 7. Cells migrated to the right chamber containing GelMA on **e** day 1, **f** day 3, **g** day 7

of 200 μg mL^{-1} was tested in two models, 2D HCC culture directly on the bottom of the bioreactor chamber in the bioreactor and 3D HCC culture in the GelMA hydrogel in the chamber. The experiments were performed statically for 4 days with TQ dissolved in the medium. As observed in Fig. S2b and c, the cell viability decreased substantially in both cases compared to the control where no TQ was administrated. However, in the case where the HepG2 cells were encapsulated inside GelMA, the toxicity exerted by TQ was moderate compared to viability decrease in the case of 2D monolayer culture, due to the retarded penetration of TQ inside the hydrogel in a diffusion-mediated manner, which is believed to be more biomimetic to the in vivo scenario. To find the appropriate concentration of encapsulated TQ, different concentrations of the nano particles ranging between 200 to 12.5 μg mL^{-1} were further placed over the HepG2 cell-encapsulated GelMA in the bottom part of the bioreactor and the experiments were conducted under static conditions (Fig. S2d). Increasing the drug concentration led to drastic decrease in the cellular viability and a concentration of 50 μg mL^{-1} at the vicinity of IC_{50} was chosen for further investigation.

Characterizations of TQ-encapsulated chitosan nanoparticles

To understand the TQ effect on the inhibition of HCC metastasis-on-chip, TQ was further encapsulated in chitosan nanoparticles. Chitosan is a natural biopolymer widely used in biomedical applications due to its biocompatibility, biodegradability, and non-toxicity [21]. As such, chitosan has also been extensively explored as carriers for sustained drug delivery [21]. The primary advantage of using this carrier system for delivering TQ lies in indirect contact of TQ with the HCC cells as well as controlled release of TQ over time, so that metastasis prevention could be better controlled. In addition, it has been reported that chitosan by itself has an anticancer effect [22], and thus, by using chitosan nanoparticles containing TQ, HCC metastasis inhibition might be enhanced in synergy with concurrent TQ release.

Characteristics of nanoparticles such as size distribution and surface properties play key roles in their cellular uptake [23]. The average sizes of empty and TQ-loaded chitosan nanoparticles were determined by dynamic light scattering (DLS) as 162.8 ± 11.65 nm and 489.3 ± 31.64 nm, respectively (Fig. 6a). The mean particle size of TQ-loaded nanoparticles was larger than that of the empty nanoparticles, as a result of reduction in chitosan/tripolyphosdphate (TPP) interaction through the incorporation of negatively charged TQ molecules leading to increase in nanoparticle sizes [24]. Polydispersity index (PDI) is the index of size distribution and presents the similarity between particle sizes. This value can range from 0 to 1, where PDI values of greater than 0.5 generally indicate relatively broad size distributions. The size and size distribution of nanoparticles directly affect the drug release rates and the therapeutic efficacy of the formu-

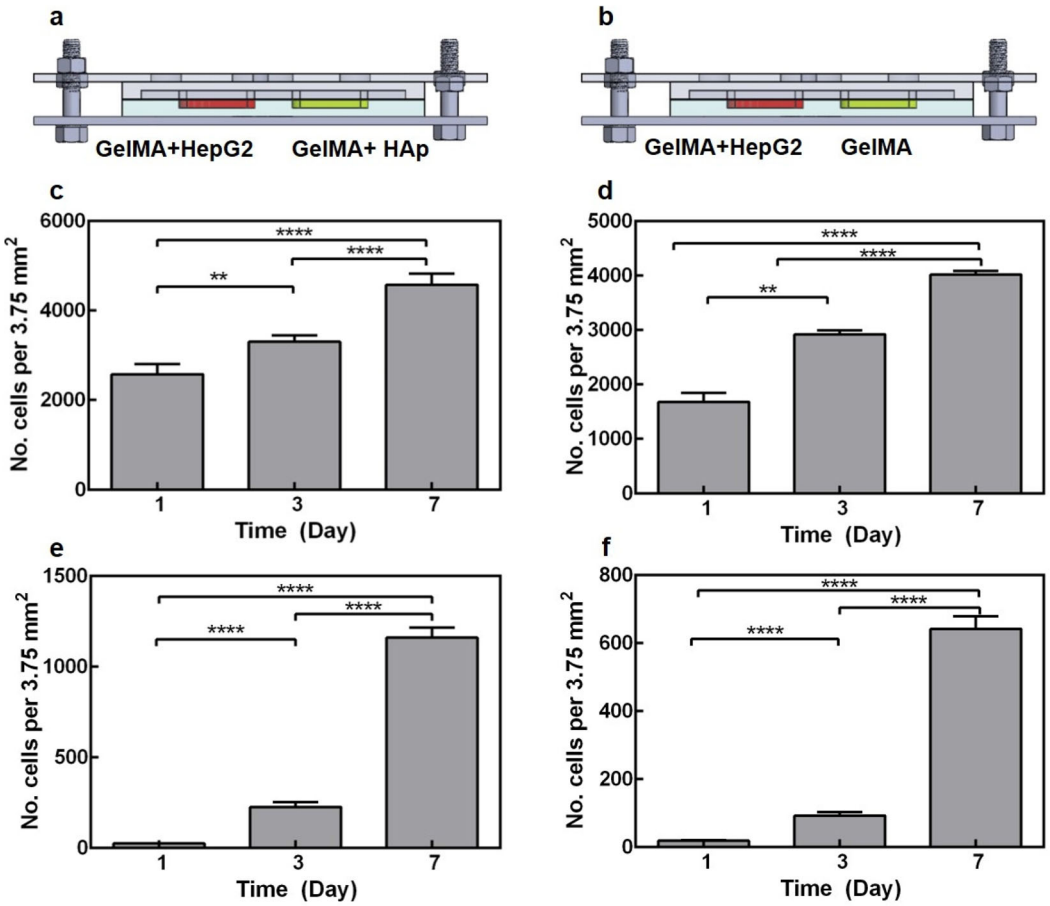

Fig. 5 Quantification of proliferated and migrated HepG2 cells. **a**, **b** Schematic representations of the bioreactor configuration containing **a** HAp or **b** pure GelMA in the metastatic chamber. **c**, **d** Quantifications of proliferated HepG2 cells in the primary tumor chambers for configurations with **c** HAp and **d** pure GelMA niches in the metastatic chambers. **e**, **f** Quantifications of metastasized HepG2 cells in the secondary chambers containing **e** HAp and **f** pure GelMA niches. ***$P < 0.0001$

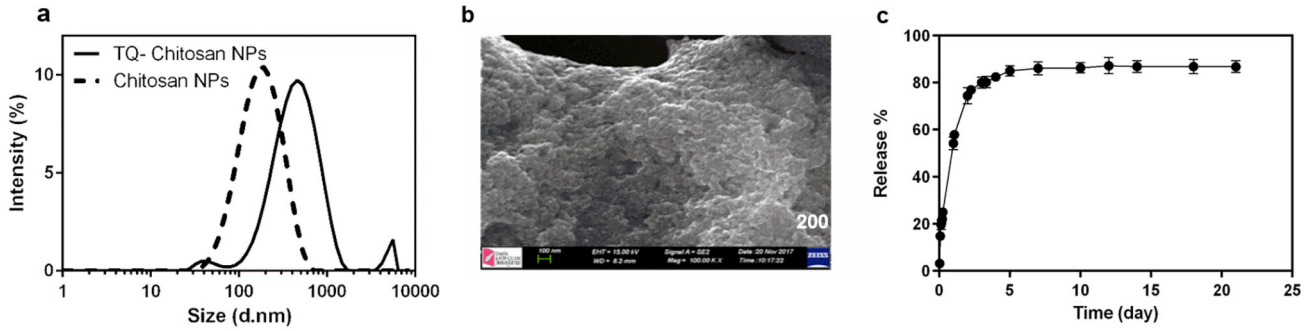

Fig. 6 Characterizations of chitosan nanoparticles. **a** Particle size distributions of empty and TQ-loaded chitosan nanoparticles measured by DLS. **b** SEM image of TQ-loaded chitosan nanoparticles. **c** FTIR spectra of free TQ, and empty and TQ-loaded chitosan nanoparticles

lations [21]. However, it is challenging to prepare chitosan nanoparticles with a narrow particle size distribution by conventional methods, which limits their suitability in certain applications [25]. The nanoparticles prepared in this study showed a narrow size distribution with 0.216 of the PDI value, ensuring uniform delivery of drug molecules from all nanoparticles. Zeta potential measures the surface charge of particles and has a significant effect on particle stability in suspensions [23, 24]. The zeta-potential values of empty and TQ-loaded nanoparticles were measured as 11.93 ± 0.45 mV

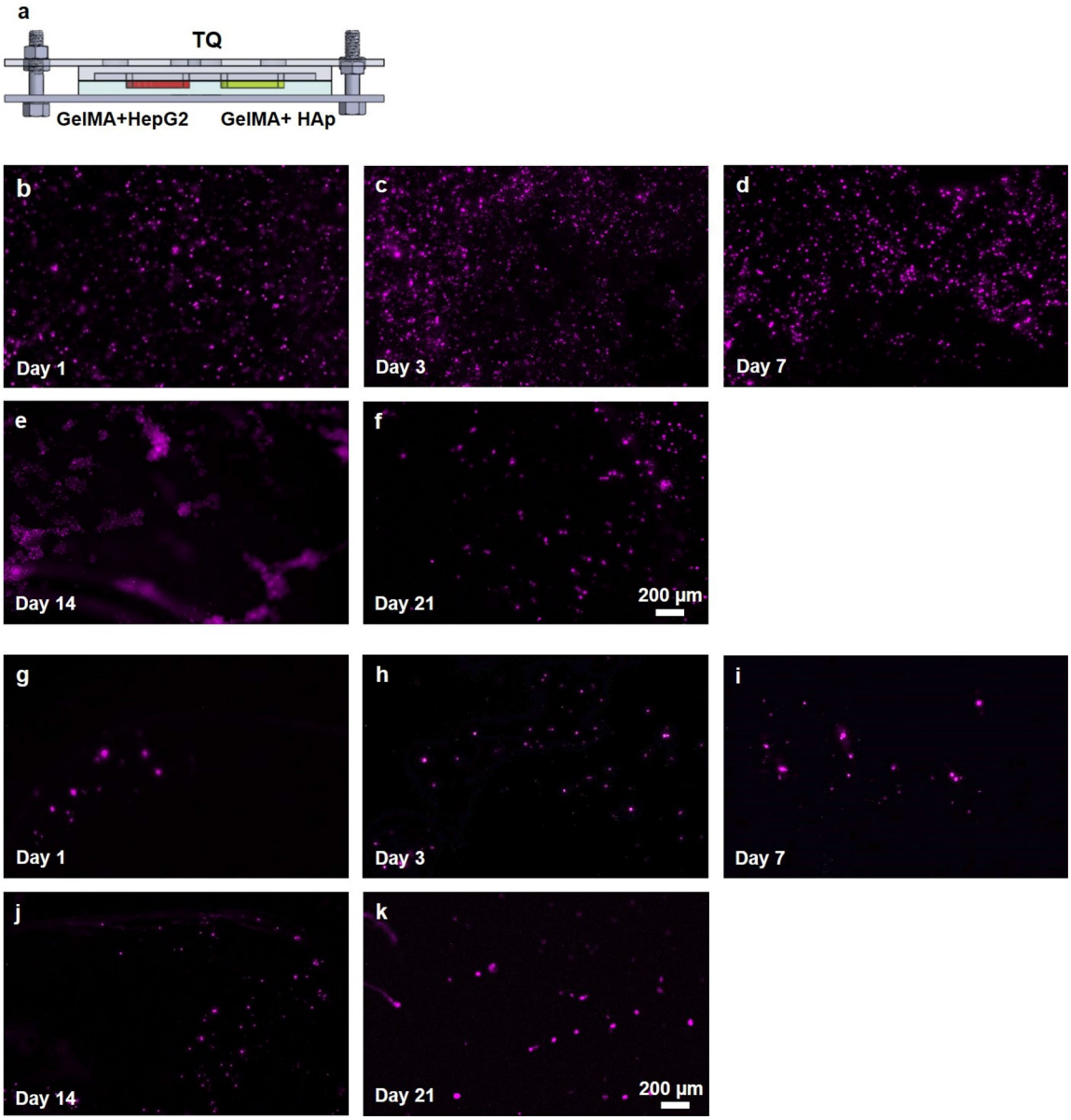

Fig. 7 Hepatocyte distribution and metastasis-on-chip in the dynamic condition under the effect of TQ. **a** Schematic of the bioreactor with encapsulated liver cancer cells in left and HAp in the right chambers, respectively. **b–f** HepG2 cells encapsulated in GelMA inside left chamber on **b** day 1, **c** day 3, **d** day 7, **e** day 14, and **f** day 21; **g–k** cells migrated to the right chamber containing GelMA and 0.1 wt% HAp on **g** day 1, **h** day 3, **i** day 7, **j** day 14, and **k** day 21

and 7.51 ± 0.43 mV, respectively. Although zeta-potential values showed a decrease with the addition of negatively charged TQ in the formulation, TQ-loaded chitosan nanoparticles still had a positive surface charge. This positive zeta potential of chitosan nanoparticles may enable the adhesion of the nanoparticles to the cells due to the electrostatic interactions between the positively charged formulation and the negatively charged cell membranes [24].

Morphological features of the nanoparticles were examined by scanning electron microscopy (SEM) (Fig. 6b), where the sizes of the nanoparticles were smaller than the hydrodynamic sizes measured by DLS. The Fourier-transform infrared (FTIR) spectrum of free TQ presented the characteristic peaks of C-H stretching at 2966 cm^{-1}, C=O bond at 1637 cm^{-1}, and C–H bending at 1245 cm^{-1}, 1131 cm^{-1}, and 1022 cm^{-1} (Fig. 6c), matching those reported in the literature [16, 19]. It was reported that chitosan has peaks at 1658 cm^{-1} and 1589 cm^{-1} referring to amide I and amino groups, respectively. As shown in Fig. 6c, the characteristic peak of chitosan at 1658 cm^{-1} disappeared

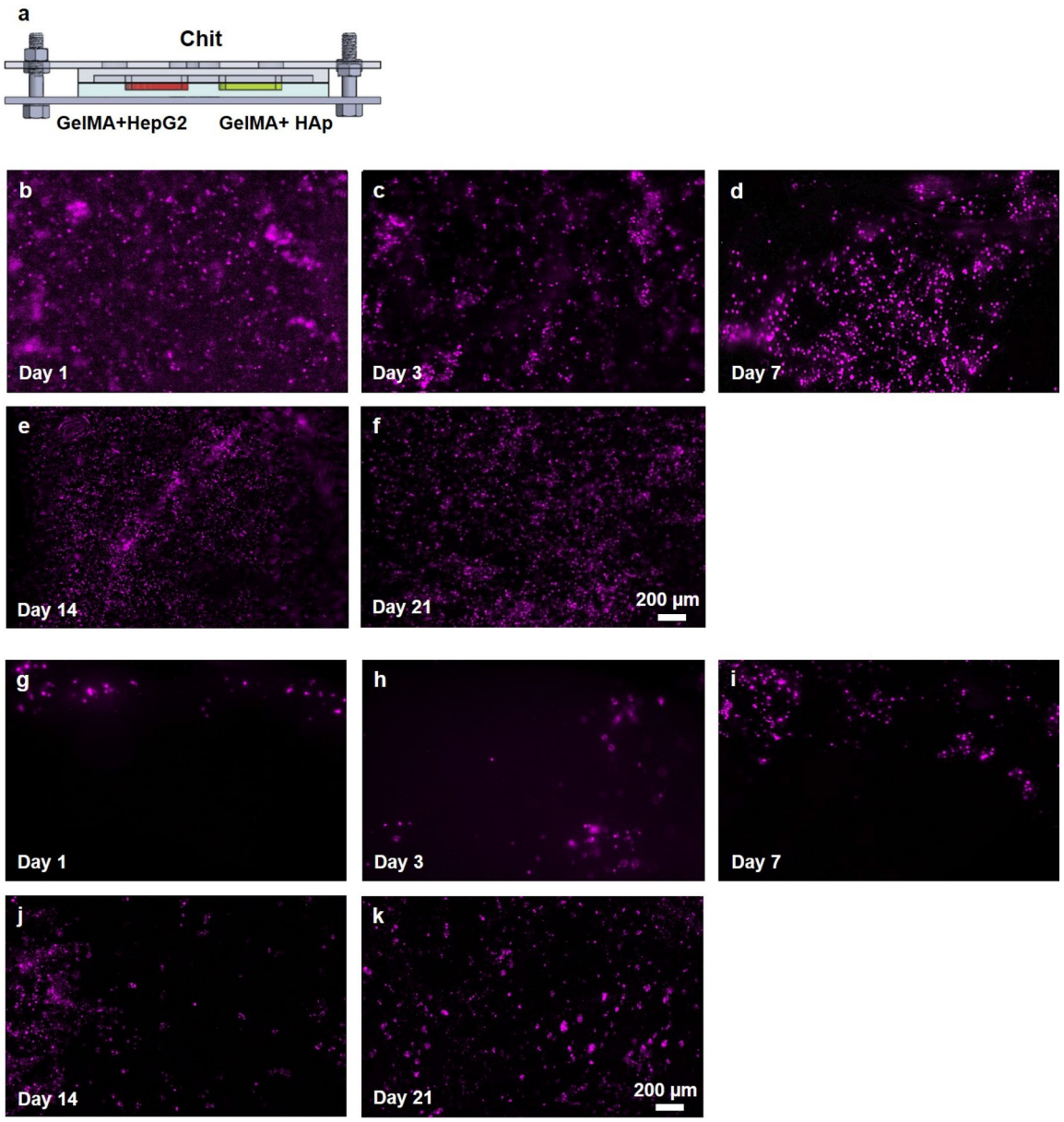

Fig. 8 Hepatocyte distribution and metastasis-on-chip in the dynamic condition with HAp under the effect of chitosan. **a** Schematic representation of the bioreactor. **b–f** HepG2 cells encapsulated in GelMA inside left chamber on **b** day 1, **c** day 3, **d** day 7, **e** day 14, and **f** day 21; **g–k** cells migrated to the right chamber containing GelMA and 0.1 wt% HAp on **g** day 1, **h** day 3, **i** day 7, **j** day 14, and **k** day 21

after nanoparticle formation. The amide II peak of chitosan at 1589 cm^{-1} was shifted to 1532 cm^{-1} as a result of electrostatic interaction formed between the NH^{3+} groups of chitosan and the phosphoric groups of TPP. The peaks at 1155 cm^{-1} and 892 cm^{-1} referred to P=O stretching and pyranose ring, while the symmetric stretching of C–O–C appeared at 1020 and 1065 cm^{-1}. FTIR spectra of empty and TQ-loaded nanoparticles were similar, indicating that there was no chemical interaction between the drug and the polymer. When the spectra of free TQ and TQ-loaded chitosan nanoparticles were analyzed, it was clear that the characteristic peaks of TQ were masked after encapsulation [26].

Differential scanning calorimeter (DSC) analyses of the samples were carried out between 20 and 350 °C, and similar curves were obtained for empty and TQ-loaded chitosan nanoparticles. In the DSC curve of free TQ, an endothermic peak corresponding to melting of TQ molecule was seen at 48.5 °C, which was absent in the DSC curve of TQ-loaded chitosan nanoparticles (Fig. S3a), suggesting that TQ was molecularly dispersed within the matrix showing the amorphous nature that further authenticated the

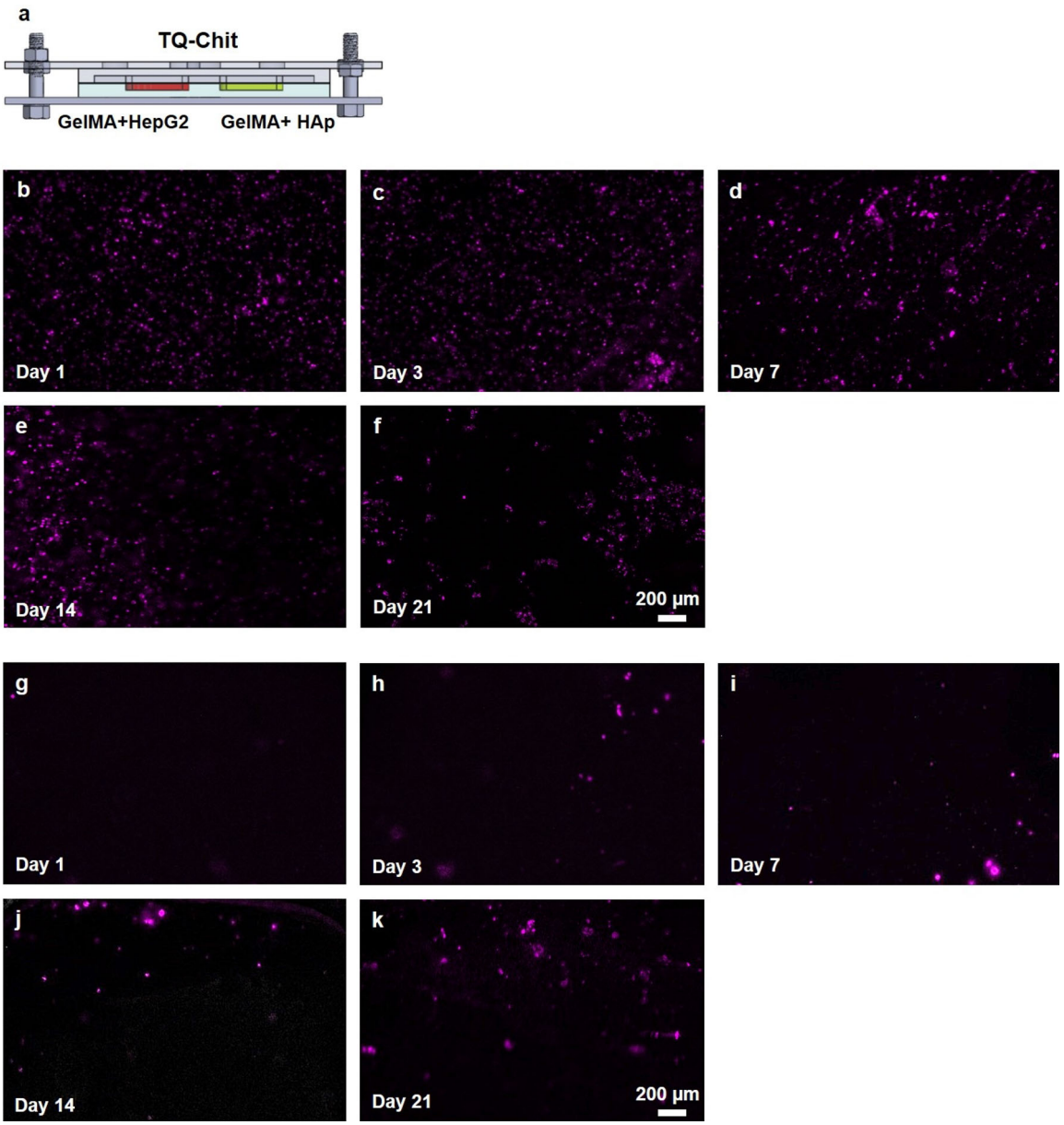

Fig. 9 Hepatocyte distribution and metastasis-on-chip in the dynamic condition under the effect of TQ-encapsulated chitosan nanoparticles. **a** Schematic representation of the bioreactor. **b**–**f** HepG2 cells encapsulated in GelMA inside left chamber on **b** day 1, **c** day 3, **d** day 7, **e** day 14, and **f** day 21; **g**–**k** cells migrated to the right chamber containing GelMA and 0.1 wt% HAp on **g** day 1, **h** day 3, **i** day 7, **j** day 14, and **k** day 21

good encapsulation of TQ. In addition, TQ-loaded chitosan nanoparticles showed a higher melting temperature than free TQ, indicating the enhanced thermal stability of TQ through encapsulation (Fig. S3a). In vitro release assessment was carried out using a standard dialysis method for 7 days and the release yield was determined as 59% (Fig. S3b). TQ concentration in the release medium showed a rapid increase in the first hours of incubation and then remained constant following the 4th day. The similar burst increase followed by sustained release was also reported in previous studies [23], where the drug present at or just beneath the surface of the nanoparticles is responsible for this effect [23]. In previous studies, TQ-loaded nanoparticles were prepared and based on the nanoparticle formulation different release yields such as 75% in 8 h [27] and 70% in 7 days [23] were demonstrated, while release profiles were similar to the profile obtained in our study. As it is seen, different release values were reported for TQ since the drug release is highly dependent on the properties of the drug and the encapsulation material, interactions, between these components, and particle synthesis

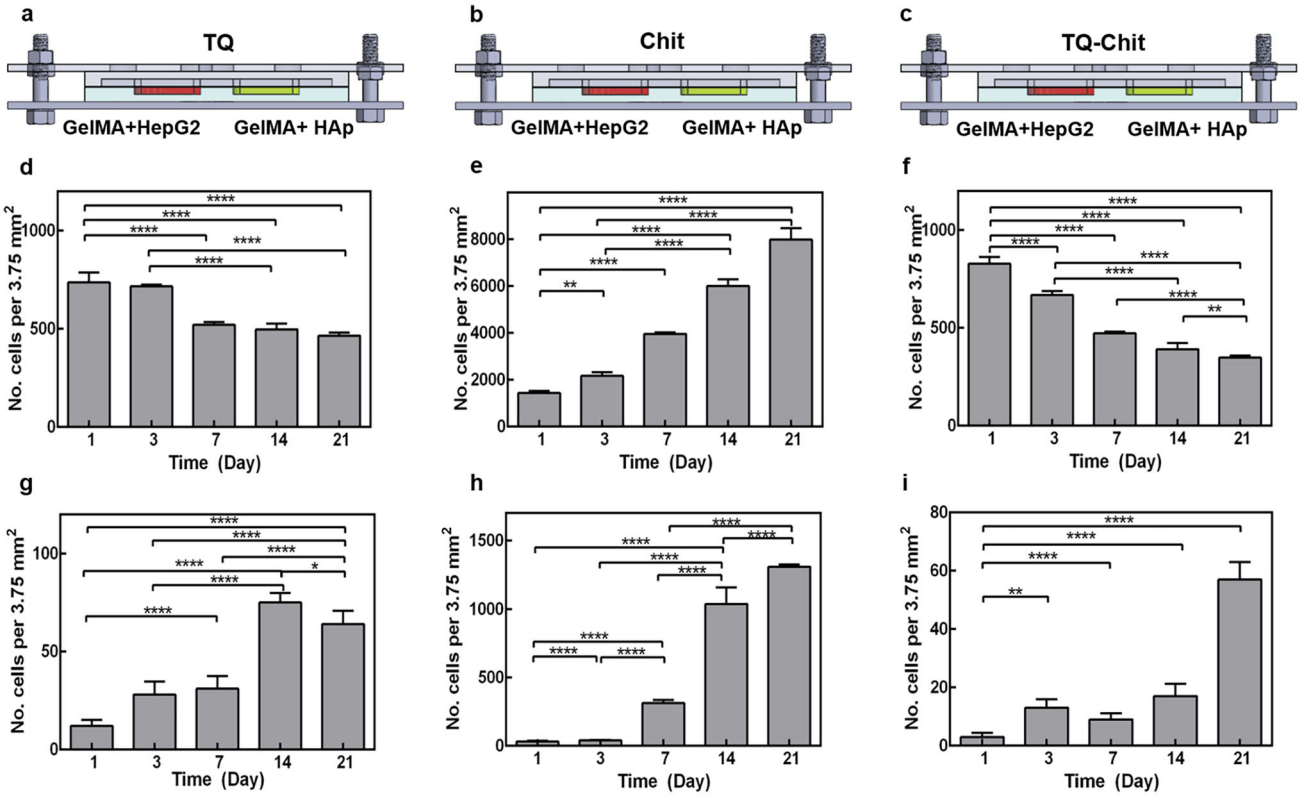

Fig. 10 Quantification of proliferated and migrated HepG2 cells under the effects of TQ, chitosan, or TQ-encapsulated chitosan nanoparticles. Schematic representations of the bioreactor configurations treated by **a** TQ, **b** chitosan, and **c** TQ-encapsulated chitosan nanoparticles. **d**–**f** Quantifications of proliferated HepG2 cells in the primary tumor chambers under the effects of **d** TQ, **e** chitosan, and **f** TQ-encapsulated chitosan nanoparticles. **g**–**i** Quantifications of metastasized HepG2 cells in the secondary chambers treated by **g** TQ, **h** chitosan, and **i** TQ-encapsulated chitosan nanoparticles. ***$P < 0.0001$

methods [23]. In this study, 86% of the encapsulated TQ was released from chitosan nanoparticles and this incomplete release might be associated with poor water-soluble nature of TQ that limited its solubility in release medium and thus potential loss of TQ during encapsulation or sampling process. The dialysis membrane could also have served as a diffusion barrier, especially for poorly water-soluble drugs, and therefore, released drug may accumulate or bind on the dialysis membrane and affect the release kinetics [28].

Inhibitory effects of on-chip HCC metastasis by TQ, chitosan, and TQ-encapsulated chitosan nanoparticles

HCC metastases toward the bone-like chamber under the effect of free TQ (Fig. 7a), chitosan nanoparticles (Fig. 8a), and TQ-encapsulated chitosan nanoparticles (Fig. 9a) were investigated for up to 21 days. It was clear that free TQ decreased cell number in the HCC chamber, revealing strong inhibition on cancerous cell proliferation (Figs. 7b–f, 10d). Conversely, HCC cell proliferation in the bioreactors under the effect of chitosan nanoparticles was undisturbed (Figs. 8b–f, 10e) and comparable to that without any treatment (Figs. 3b–d, 5d), suggesting the non-toxicity of the chitosan nanoparticles themselves. When TQ-encapsulated chitosan nanoparticles were infused through the vascular circulation however, inhibition was again observed showing reduced cell density over the culture period (Figs. 9b–f, 10f). These data highlighted a remarkable reduction in HCC growth with both TQ and TQ-encapsulated chitosan nanoparticles, while the latter had slightly more extended effective duration leading to lower cell number at the end of 21-day culture possibly due to the controlled release of TQ from the nanoparticle formulation (Fig. 10d–f).

On the other hand, a similar trend on the metastatic HCC cells in response to the different treatments was also noticed. When treated with free TQ (Figs. 7g–k, 10g) or TQ-encapsulated chitosan nanoparticles (Figs. 9g–k, 10i), the numbers of HCC cells that settled at the secondary bone-like site were significantly lower than those in the chitosan treatment (Fig. 8g–k, 10h) or non-treatment group (Figs. 3e–g, 5f). Matching the differential HCC growth profiles, TQ-encapsulated chitosan nanoparticles had seemed to result in overall lower metastatic cell numbers than free TQ, further confirming the possible effects facilitated by sustained release of the molecule (Fig. 10g–i).

Discussion

In this study, a platform for modeling the metastasis of HCC to the bone was presented, in which HepG2 cells were encapsulated in the GelMA hydrogel in a microtissue compartment and HAp was encapsulated within the GelMA matrix in the second compartment mimicking the bone niche inside our model. A porous membrane was placed over these two compartments resembling vascular barrier in the upper section of the bioreactor. Medium flow was circulated over the vascular membrane. HCC–bone metastasis-on-a-chip device was run up to several weeks. It was observed that HepG2 cells were migrated to the secondary bone site in a mineral-dependent manner.

This HCC–bone metastasis-on-a-chip device further provided a unique platform to evaluate the effects of anticancer drugs in both free form and when encapsulated in particulate delivery systems. In particular, an herbal metastasis-prohibitive compound, TQ, was used in free and chitosan-encapsulated nanoparticle forms as a repressive factor of HCC metastasis. The obtained results showed that the TQ-encapsulated nanoparticles could inhibit HCC metastasis for longer duration in comparison with the case in which free molecules were administrated.

The in vitro model developed here for investigation of HCC-to-bone metastasis can be useful to be applied to similar metastasis applications in which the process of the invasion, the stimuli accelerating its trigger, and the effects of inhibitory medicines can be scrutinized. Moreover, this metastasis-on-chip platform can be personalized, which can precipitate the process of finding the suitable anticancer medicine for a specific patient. With further optimizations, we anticipate this platform to facilitate more accurate drug screening, personalized medicine, and toxicology studies in the future.

Funding This work was supported by the National Institutes of Health (K99CA201603, R00CA201603, R21EB025270, R21EB026175, R01EB028143), the New England Anti-Vivisection Society, and the Brigham Research Institute.

Availability of data and material (data transparency) The datasets that support the findings of this study are available from the corresponding authors upon reasonable request. All requests for raw and analyzed data and materials will be promptly reviewed by the Brigham and Women's Hospital to verify whether the request is subject to any intellectual property or confidentiality obligations. Any data and materials that can be shared will be released via a Material Transfer Agreement.

Compliance with ethical standards

Conflict of interest The authors declare no conflict of interest.

Consent to participate Consent to participate is not applicable in this study.

Consent for publication All authors have reviewed and approved the manuscript.

Ethics approval Ethical approval is not applicable in this study.

References

1. Society AC (2015) Global cancer facts & figures, 3rd edn. American Cancer Society, Atlanta
2. Portillo-Lara R, Annabi N (2016) Microengineered cancer-on-a-chip platforms to study the metastatic microenvironment. Lab Chip 16(21):4063–4081
3. Sharifi F, Firoozabadi B, Firoozbakhsh K (2019) Numerical investigations of hepatic spheroids metabolic reactions in a perfusion bioreactor. Front Bioeng Biotechnol 7:221
4. Sharifi F, Htwe SS, Righi M, Liu H, Pietralunga A, Yesil-Celiktas O, Maharjan S, Cha BH, Shin SR, Dokmeci MR (2019) A foreign body response-on-a-chip platform. Adv Healthc Mater 8(4):1801425
5. Kong J, Luo Y, Jin D, An F, Zhang W, Liu L, Li J, Fang S, Li X, Yang X (2016) A novel microfluidic model can mimic organ-specific metastasis of circulating tumor cells. Oncotarget 7(48):78421
6. Ananthakrishnan A, Gogineni V, Saeian K (2006) Epidemiology of primary and secondary liver cancers. Semin Intervent Radiol 23(1):47–63
7. Katyal S, Oliver JH III, Peterson MS, Ferris JV, Carr BS, Baron RL (2000) Extrahepatic metastases of hepatocellular carcinoma. Radiology 216(3):698–703
8. Ng J, Shin Y, Chung S (2012) Microfluidic platforms for the study of cancer metastasis. Biomed Eng Lett 2(2):72–77
9. Skardal A, Shupe T, Atala A (2016) Organoid-on-a-chip and body-on-a-chip systems for drug screening and disease modeling. Drug Discov Today 21(9):1399–1411
10. Bersini S, Jeon JS, Dubini G, Arrigoni C, Chung S, Charest JL, Moretti M, Kamm RD (2014) A microfluidic 3D in vitro model for specificity of breast cancer metastasis to bone. Biomaterials 35(8):2454–2461
11. Bischel LL, Casavant BP, Young PA, Eliceiri KW, Basu HS, Beebe DJ (2014) A microfluidic coculture and multiphoton FAD analysis assay provides insight into the influence of the bone microenvironment on prostate cancer cells. Integr Biol 6(6):627–635
12. Zuchowska A, Kwapiszewska K, Chudy M, Dybko A, Brzozka Z (2017) Studies of anticancer drug cytotoxicity based on long-term HepG2 spheroid culture in a microfluidic system. Electrophoresis 38(8):1206–1216
13. Breuksch I, Weinert M, Brenner W (2016) The role of extracellular calcium in bone metastasis. J Bone Oncol 5(3):143–145
14. Joyce JA, Pollard JW (2009) Microenvironmental regulation of metastasis. Nat Rev Cancer 9(4):239
15. Khader M, Eckl PM (2014) Thymoquinone: an emerging natural drug with a wide range of medical applications. Iran J Basic Med Sci 17(12):950
16. Loessner D, Meinert C, Kaemmerer E, Martine LC, Yue K, Levett PA, Klein TJ, Melchels FP, Khademhosseini A, Hutmacher DW (2016) Functionalization, preparation and use of cell-laden gelatin methacryloyl–based hydrogels as modular tissue culture platforms. Nat Protoc 11(4):727
17. Xavier JR, Thakur T, Desai P, Jaiswal MK, Sears N, Cosgriff-Hernandez E, Kaunas R, Gaharwar AK (2015) Bioactive nanoengineered hydrogels for bone tissue engineering: a growth-factor-free approach. ACS Nano 9(3):3109–3118
18. Yeh W-C, Li P-C, Jeng Y-M, Hsu H-C, Kuo P-L, Li M-L, Yang P-M, Lee PH (2002) Elastic modulus measurements of human liver and correlation with pathology. Ultrasound Med Biol 28(4):467–474

19. Ma X, Qu X, Zhu W, Li Y-S, Yuan S, Zhang H, Liu J, Wang P, Lai CSE, Zanella F (2016) Deterministically patterned biomimetic human iPSC-derived hepatic model via rapid 3D bioprinting. Proc Natl Acad Sci 113(8):2206–2211
20. Olechnowicz SW, Edwards CM (2014) Contributions of the host microenvironment to cancer-induced bone disease. Can Res 74(6):1625–1631
21. Sinha V, Singla A, Wadhawan S, Kaushik R, Kumria R, Bansal K, Dhawan S (2004) Chitosan microspheres as a potential carrier for drugs. Int J Pharm 274(1):1–33
22. Karagozlu MZ, Kim S-K (2015) Anti-cancer effects of chitin and Chitosan derivatives. In: Kim S-K (ed) Handbook of anticancer drugs from marine origin. Springer, pp 413–421
23. Soni P, Kaur J, Tikoo K (2015) Dual drug-loaded paclitaxel–thymoquinone nanoparticles for effective breast cancer therapy. J Nanopart Res 17(1):18
24. He C, Hu Y, Yin L, Tang C, Yin C (2010) Effects of particle size and surface charge on cellular uptake and biodistribution of polymeric nanoparticles. Biomaterials 31(13):3657–3666
25. Fan W, Yan W, Xu Z, Ni H (2012) Formation mechanism of monodisperse, low molecular weight chitosan nanoparticles by ionic gelation technique. Colloids Surf B 90:21–27
26. Hosseini SF, Zandi M, Rezaei M, Farahmandghavi F (2013) Two-step method for encapsulation of oregano essential oil in chitosan nanoparticles: preparation, characterization and in vitro release study. Carbohydr Polym 95(1):50–56
27. Ganea GM, Fakayode SO, Losso JN, Van Nostrum CF, Sabliov CM, Warner IM (2010) Delivery of phytochemical thymoquinone using molecular micelle modified poly (D, L lactide-co-glycolide)(PLGA) nanoparticles. Nanotechnology 21(28):285104
28. Abouelmagd SA, Sun B, Chang AC, Ku YJ, Yeo Y (2015) Release kinetics study of poorly water-soluble drugs from nanoparticles: are we doing it right? Mol Pharm 12(3):997–1003